© 2017. Published by The Company of Biologists Ltd | Development (2017) 144, 1087-1096 doi:10.1242/dev.140228

STEM CELLS AND REGENERATION

RESEARCH ARTICLE

Self-organisation after embryonic kidney dissociation is driven via selective adhesion of ureteric epithelial cells

James G. Lefevre[1,*,‡], Han S. Chiu[1,*], Alexander N. Combes[1,2,3], Jessica M. Vanslambrouck[1,3], Ali Ju[1,4], Nicholas A. Hamilton[1] and Melissa H. Little[1,3,5]

ABSTRACT

Human pluripotent stem cells, after directed differentiation *in vitro*, can spontaneously generate complex tissues via self-organisation of the component cells. Self-organisation can also reform embryonic organ structure after tissue disruption. It has previously been demonstrated that dissociated embryonic kidneys can recreate component epithelial and mesenchymal relationships sufficient to allow continued kidney morphogenesis. Here, we investigate the timing and underlying mechanisms driving self-organisation after dissociation of the embryonic kidney using time-lapse imaging, high-resolution confocal analyses and mathematical modelling. Organotypic self-organisation sufficient for nephron initiation was observed within a 24 h period. This involved cell movement, with structure emerging after the clustering of ureteric epithelial cells, a process consistent with models of random cell movement with preferential cell adhesion. Ureteric epithelialisation rapidly followed the formation of ureteric cell clusters with the reformation of nephron-forming niches representing a later event. Disruption of P-cadherin interactions was seen to impair this ureteric epithelial cell clustering without affecting epithelial maturation. This understanding could facilitate improved regulation of patterning within organoids and facilitate kidney engineering approaches guided by cell-cell self-organisation.

KEY WORDS: Self-organisation, Morphogenesis, Cell adhesion

INTRODUCTION

Self-organisation can be defined as the creation of a structure from component parts without external direction, scaffold or template. Self-organisation in the context of development refers to the capacity of the embryo to form complex tissues from component cell types. This is assumed to result from complex cell-cell interactions that direct competence, fate, induction, movement and relative cellular interactions. Self-organisation in tissue morphogenesis has long been described, including studies on the reformation of sponges after cell dispersal (Wilson, 1907) and embryonic lungs after disaggregation (Trinkaus and Groves, 1955; Grover, 1963). It is proposed that such self-organisation involves cell chemotaxis (Bonner, 1947) and cell sorting based on differential cell adhesion (Holtfreter, 1939, 1943); however, there have been few mechanistic studies investigating this in detail in any organism. The relevance of self-organisation has seen a recent rebirth with the observations that organotypic structures – referred to as organoids – can arise *in vitro* after the directed differentiation of pluripotent stem cells. This does not seem to require anything other than the provision of signals to mimic the required component germ layer or tissue-specific progenitors from the starting stem cells and the provision of a 3D environment. Within such organoids, complex mixtures of tissue progenitors self-organise themselves in a manner akin to that occurring during development, although the process by which this occurs cannot be taken as representing normal development. In this way, the formation of optic cup, adenohypophysis, cerebral cortex, intestine, stomach and kidney have now been generated from human pluripotent stem cells (Eiraku et al., 2011; Suga et al., 2011; Spence et al., 2011; Lancaster et al., 2013; McCracken et al., 2014; Takasato et al., 2015; reviewed in Ader and Tanaka 2014).

Tissue organoids provide an unprecedented opportunity to model human development. However, although the resulting structures have been described, the mechanisms by which organoids form *in vitro* remains poorly characterised. Tissue organoids generated from pluripotent stem cells often arise from embryoid body cultures, presumably as a result of morphogenetic patterning within three-dimensional space involving distinct component cell populations. We have previously reported a protocol for the generation of kidney organoids in which an initial period of monolayer induced pluripotent stem cell (iPSC) culture is followed by total cell dissociation and reaggregation (Takasato et al., 2015). Here, component cells must self-organise to reconstruct form without prior spatial information. A capacity for the embryonic kidney to reform after dissociation was reported in the chick more than 50 years ago (Weiss and Taylor, 1960). The resulting reaggregates contained collecting duct and appropriately patterned nephrons with glomeruli and renal tubules. More recently, we and others have reported that murine embryonic kidney between 11.5 and 13.5 days post-coitum (dpc) can be enzymatically dissociated to a single-cell suspension, reaggregated as a pellet and cultured on a floating filter at an air–media interface (Unbekandt and Davies, 2010; Lusis et al., 2010) (Fig. 1B). After 4-6 days of culture, the resulting aggregates reform collecting duct epithelium surrounded by nephron progenitors that give rise to nascent nephrons (Unbekandt and Davies, 2010; Lusis et al., 2010; Davies et al., 2012; Hendry et al., 2013). This approach of dissociation and reaggregation of embryonic tissue serves as an appropriate experimental system within which to investigate how this occurs.

Using confocal time-lapse imaging, 3D confocal reconstruction and mathematical modelling, this study has analysed *in vitro* self-organisation using reaggregation of dissociated embryonic mouse kidney. This reveals a process in which the collecting duct cells

[1]Institute for Molecular Bioscience, The University of Queensland, St. Lucia, Brisbane 4072, Australia. [2]Department of Anatomy and Neuroscience, Faculty of Science, University of Melbourne, Parkville 3052, Australia. [3]Murdoch Children's Research Institute, Parkville, Melbourne 3052, Australia. [4]Translational Research Institute, Woolloongabba, Brisbane 4102, Australia. [5]Department of Pediatrics, Faculty of Medicine, Dentistry and Health Sciences, University of Melbourne, Parkville 3052, Australia.
*These authors contributed equally to this work

‡Author for correspondence (j.lefevre@uq.edu.au)

J.G.L., 0000-0002-5945-9575; A.N.C., 0000-0001-6008-8786; N.A.H., 0000-0003-0331-3427; M.H.L., 0000-0003-0380-2263

Received 23 May 2016; Accepted 12 January 2017

Development (2017) 144, 1087-1096 doi:10.1242/dev.140228

rapidly reform epithelial structures via differential cadherin-based cell-cell adhesion, with nephron formation a subsequent event.

RESULTS

Defining the temporal nature of self-organisation after embryonic kidney dissociation and reaggregation

The mammalian kidney forms through reciprocal interactions between instructive cell populations. The best characterised of these are the ureteric epithelial population and the metanephric mesenchymal population (Little and McMahon, 2012). The ureteric epithelium (UE), in response to GDNF secreted by the mesenchyme, undergoes iterative dichotomous branching to form the collecting ducts of the organ (Little and McMahon, 2012; Short et al., 2014). The mesenchyme most closely associated with the tip of the UE, referred to as the cap mesenchyme (CM), represents a self-renewing progenitor population that both drives the branching of the UE as well as forming the functional epithelial units of the kidney, the nephrons (Kobayashi et al., 2008; Boyle et al., 2008). These nephrons are formed from the CM by means of a mesenchyme-to-epithelial transition (MET) as a result of signals from the UE tips (Carroll et al., 2005). Hence, the morphogenetic niches of the organ consist of the tips of the branching UE and the surrounding CM (Fig. 1A). We have previously observed the recreation of such niches within *in vitro* reaggreation cultures (Hendry et al., 2013).

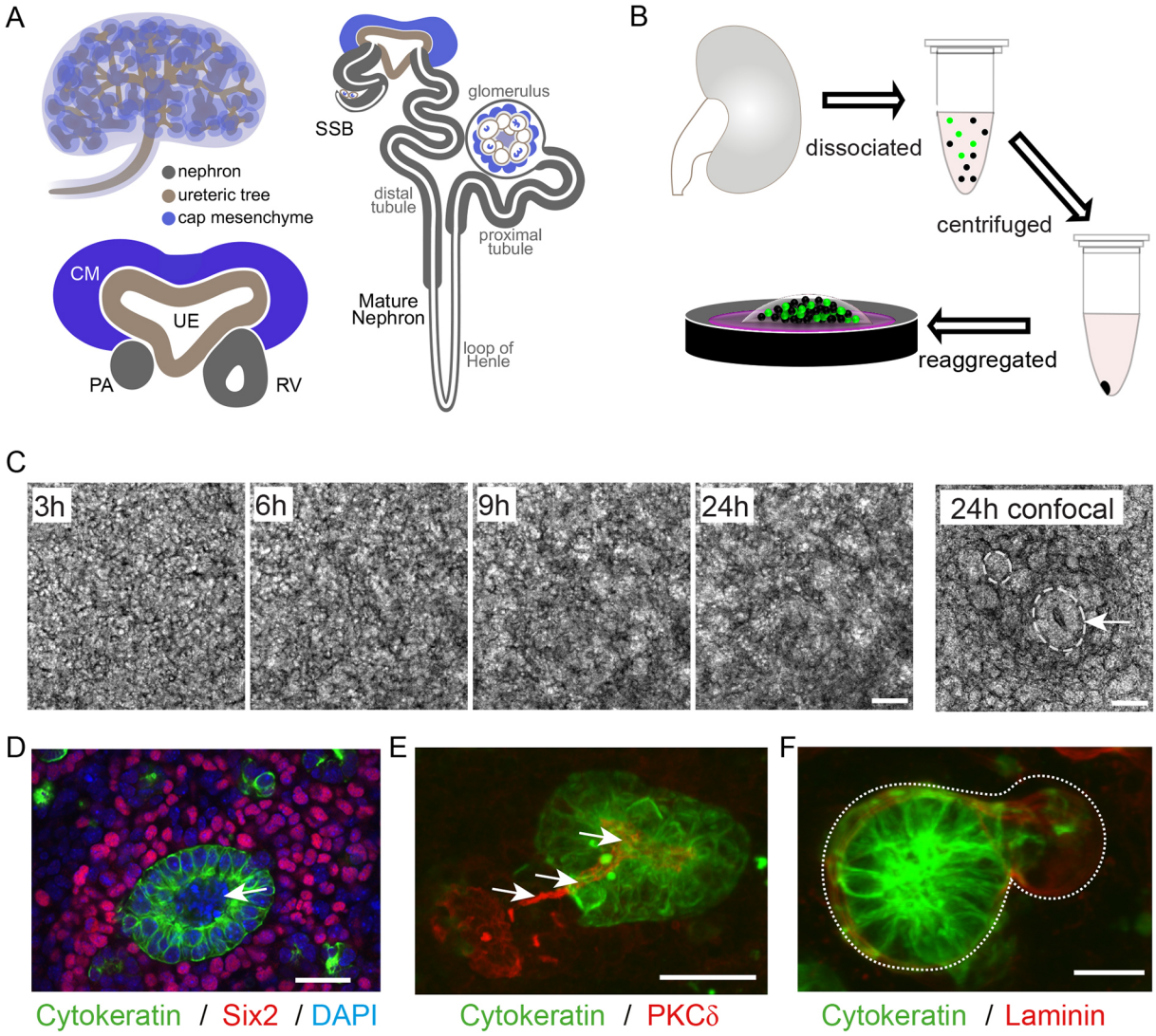

Fig. 1. Kidney morphogenesis *in vitro* after dissociation of embryonic kidneys. (A) Diagram of normal murine kidney morphogenesis showing the mid-gestational kidney (top left) below which is a magnified view of a nephrogenic niche identifying the branching ureteric epithelium (UE) surrounded by the nephron progenitor of the cap mesenchyme (CM). Reciprocal signalling between the CM and the tips of the branching UE maintains branching and supports self-renewal of the CM. Signals from the UE also trigger the commitment of CM cells to nephron formation. This results in the formation of a pretubular aggregate (PA), which undergoes a mesenchyme-to-epithelial transition to form the first stage of nephron formation, the renal vesicle (RV). The RV elongates to form an S-shaped body (SSB), simultaneously fusing with the adjacent ureteric tip. The SSB then segments and vascularises to form the nephron. (B) Diagram of the reaggregation assay. (C) Brightfield timecourse of embryonic kidney reaggregation culture followed by confocal reflection microscopy to reveal internal epithelial structures. Dashed lines indicate example structures; arrow indicates a structure with visible lumen. (D-F) Immunofluorescent labelling of structures formed after 24 h of culture. (D) UE (cytokeratin$^+$; green) surrounded by nephrogenic CM (Six2$^+$; red). Arrow indicates lumen. (E) Formation of an early nephron. Arrows indicate the lumen of an early nephron connected to the UE lumen. The forming nephron connects with the UE to make a patent connecting lumen from the late renal vesicle stage of maturation (Georgas et al., 2009). UE (cytokeratin$^+$; green) and apical surface of epithelium of UE and nephron (Pkcδ$^+$; red). (F) Formation of basement membrane (white dashed line) around UE and attached early nephron. UE (cytokeratin$^+$; green) and basement membrane (laminin$^+$; red). Scale bars: 50 µm in C; 30 µm in D-F.

Development (2017) 144, 1087-1096 doi:10.1242/dev.140228

In order to investigate the timing of such self-organisation events, here, we monitored reaggregation cultures using wide-field microscopy across a 24 h timecourse (Fig. 1; Fig. S1). Two distinct approaches have previously been reported for the dissociation and reaggregation of murine embryonic kidneys (Unbekandt and Davies, 2010; Lusis et al., 2010). In this study, we have employed an adaptation of our previously reported approach (Lusis et al., 2010) in which embryonic kidneys of 13.5 dpc are dissociated, but plating after reaggregation is performed directly onto Transwell filters in the absence of both a Wnt4-secreting feeder layer (Lusis et al., 2010; Hendry et al., 2013) and transient culture with ROCKi (Unbekandt and Davies, 2010). Cell reorganisation was evident from 8 h with the presence of 'rosettes' at 24 h (Fig. 1C), suggestive of the reformation of epithelial structures. Immunofluorescent labelling after 24 h revealed the presence of polarised UE (cytokeratin^{+}) within areas of CM (Six2^{+}) (Fig. 1D). Nephron initiation was present as seen by the presence of cytokeratin^{-} tubular structures attached to the UE (Fig. 1E,F; Fig. S1).

Self-organisation requires cell movement

The speed with which such organotypic structures arose suggested either a capacity for the component cells to move and/or a capacity for these cells to switch fate to adopt a new identity. To investigate these options, we generated reaggregation cultures from triple transgenic (Six2TGC:tdTomato:Hoxb7GFP) mice (Srinivas et al., 1999; Kobayashi et al., 2008) in which the UE is labelled with green fluorescent protein (GFP) and the nephron-forming CM is labelled with Tomato fluorescent protein. In the case of the CM, labelling reflects lineage as any cell that has expressed the CM marker, Six2, will remain red even if it adopts a distinct fate (Kobayashi et al., 2008). Self-organisation *in vitro* was monitored at 8 min intervals for a period of 7 h using time-lapse confocal microscopy (Movie 1). Substantial motility was seen by both UE and CM cells (Fig. 2A-F; Movie 1). To quantify motility, individual cell trajectories were identified for each of these two cell types and the displacement of cells between consecutive time points calculated. An analysis of cell trajectories shows that the motion being observed is non-directional with the velocity distributions consistent with a bivariate Gaussian behaviour (Fig. 2C,F). This suggests random cellular movement across this period of time.

Successful self-organisation within a kidney organoid requires cells with appropriate cellular identity and competence to respond. Hence, inappropriate cell types do not contribute to structure or disrupt the process of kidney self-organisation (Hendry et al., 2011). However, this does not prove that component cell types do not change fate during self-organisation. Initial studies mixing unlabelled dissociated embryonic kidney with CM isolated from Sall1-GFP^{+} embryonic kidneys (Takasato et al., 2004) showed the selective integration of GFP^{+} cells into the CM, suggesting no loss of cell identity (Hendry et al., 2011). Using reaggregates generated from the Six2TGC:tdTomato:Hoxb7GFP triple transgenic mouse strain, an analysis of cell identity within the UE after 8 h revealed no evidence for Tomato-labelled cells forming UE structures (Fig. 2G). By 24 h post-reaggreation, focal patches of CM-derived cells were present within UE structures (Fig. 2H). In all cases these were nascent renal vesicles, representing CM-derived nephrons. These data support a model in which switching of cell fate does not occur.

Differential clustering of ureteric epithelial cells within reaggregates

The recreation of spatial niches in which a ureteric epithelial structure is surrounded by CM clearly occurs even after dissociation and reaggregation. To address which population clustered first, wild-type embryonic kidneys were subjected to dissociation and reaggregation, then cultured for 2, 8, 12, 24 and 48 h. Immunofluorescence was performed to identify the location of individual UE (cytokeratin^{+}, green) and CM (Six2^{+}, red) cells (Fig. 3A). Clusters of UE were apparent from 8 h. The location of each cell within a confocal *z*-stack was determined and the coordinates used to evaluate clustering using a Ripley's *K* algorithm applied in three dimensions (Fig. S2B,C). Ripley's *K* is used to quantify and detect non-random clustering by measuring the relative proximity of points, in this case cells, compared with randomly distributed cells of the same overall density (Fig. 3B). This analysis showed evidence for UE clustering [$K/E(K)>1$, with $E(K)$ the expected value of K under random distribution] within 8 h of reaggregation (Fig. 3C). The CM, in contrast, did not show evidence for clustering until 48 h after reaggregation (Fig. 3D). Although clustering invokes an active process, it should be noted that the density of CM cells within the cultures declines steadily across the duration of the cultures (Fig. 3E), and the median distance between Six2^{+} cells does not decrease significantly. As clustering is only evident after 48 h, we could speculate that it is also possible that CM cells do not survive unless they are within a certain distance of the UE. It is known that the CM requires growth factors from the UE for competence (Karner et al., 2011; Little and McMahon, 2012; Barak et al., 2012). This decline in CM suggests that a niche capable of supporting the CM is not present at the commencement of culture.

Modelling suggests random cell movement with differential adhesion

With the identification of specific cell-cell adhesion proteins, including the cadherins, it was proposed that homophilic cadherin interactions might explain tissue self-organisation (Steinberg, 1962, 1970; Steinberg and Takeichi, 1994; Foty et al., 1996). We hypothesised that the initial clustering of UE cells represented undirected cell motility (Brownian motion) coupled with adhesion between adjacent UE cells, rather than directed movement or change of cell identity. To test this assumption, we developed a stochastic cell simulation model incorporating random motion, local repulsion forces preventing simulated cells from occupying the same space, and adhesion forces (Fig. 4A). In this model, adhesion bonds are formed probabilistically only between pairs of proximate-like cells. Once two cells adhere to each other, this acts to prevent these cells from moving apart. As we are assuming such differential adhesion is most likely between epithelial cell types, namely the UE cells, the simulation was calibrated to the experimental conditions using the rate of Brownian motion calculated from analysis of live imaging (Fig. 2), the observed density of cytokeratin-positive cells in culture (Fig. 3), and the mean distance between all cells within the culture (Fig. S2D-F). Running this simulation showed the time-dependent formation of UE clusters (Fig. 4B; Movie 2). This allowed a comparison of the behaviour observed in the model with respect to Ripley's *K* (Fig. 4C) and cluster size distribution (Fig. 4D) of UE cells across time. This comparison showed a similar progression of UE clustering between the simulated and observed data out to 24 h, supporting the model. There was a deviation between the model and observed data at 48 h with the simulated data suggesting a continued increase in UE cluster size. This might suggest a phase change as the reclustered UE cells polarise and form lumens, as discussed in the following section. However, for the first 24 h, the modelling data support a process in which UE cells cluster as a result of differential adhesion.

Development (2017) 144, 1087-1096 doi:10.1242/dev.140228

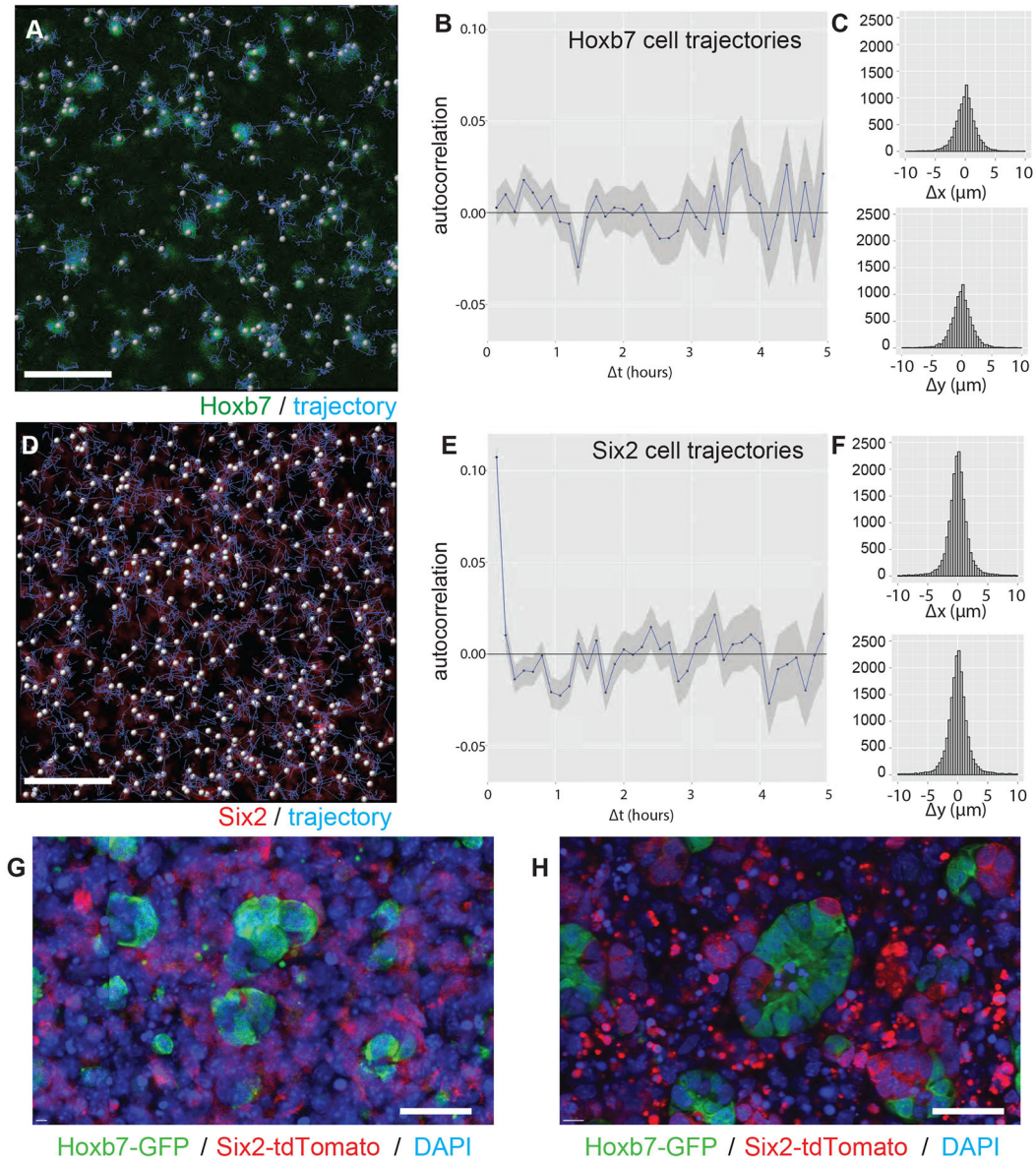

Fig. 2. Self-organisation involves cell motility rather than changes in cell fate. (A-F) Analysis of live imaging of ureteric epithelial cells (A-C) and cap mesenchymal cells (D-F) within a reaggregation culture generated from 13.5 dpc embryonic kidneys isolated from triple transgenic Six2GCE:TdTomato: Hoxb7GFP mice. Imaging was performed for a total of 7 h commencing 2 h after initial reaggregation. (A,D) Still shots from within time-lapse imaging of cultures illustrating individual cells (spot identified using Imaris software) and trajectories for each cell at each 8 min time step across the timecourse. (A) Ureteric epithelial cells (GFP^+; green). (D) CM cells ($Six2^+$; red). (B,E) Velocity autocorrelation for UE (B) and CM (E) cells; mean±s.e.m. Using calculated trajectories, cell velocities are approximated using finite differences (displacement over 8 min), and autocorrelations calculated assuming a stationary (time-invariant) process. There is clear autocorrelation at consecutive time steps for CM cells ($P<2\times10^{-12}$ by two-tailed *t*-test), but there is no detectable autocorrelation for UT cells or for CM cells at differences of three or more time steps (24 min). Calculations are based on *x* and *y* coordinates only due to reduced *z* resolution. (C,F) Distribution of velocity estimates consistent with bivariate Gaussian for both UE (C) and CM cells (F). (G,H) Analysis of cell fate across time at 8 h (G) and 24 h (H) after commencement of reaggregation culture. Immunofluorescence for Hoxb7-GFP (green) and Six2-tdTomato (red) was used to identify UE- and CM-derived cells, respectively. DAPI (blue) marks nuclei. Scale bars: 30 μm.

Blocking P-cadherin interferes with ureteric epithelial clustering, but not maturation

The disruption of cadherins during development can perturb key developmental processes, including gastrulation, epiboly and neural crest migration, each of which are associated with switches in the expression of cadherins (Niessen et al., 2011). An analysis of the expression of cadherins within the developing kidney (http://www.gudmap.org/; Harding et al., 2011; Combes et al., 2015) suggests that the UE expresses both E-cadherin (cadherin 1; Cdh1) and P-cadherin (cadherin 3; Cdh3) whereas the CM expresses N-cadherin (cadherin 2; Cdh2) and OB-cadherin (cadherin 11; Cdh11) (Fig. S3A). R-cadherin (cadherin 4; Cdh4), although also expressed in the UE, is more highly expressed in the developing nephrons. Antibody staining of 13.5 dpc developing mouse kidney confirmed the presence of Cdh3 in the ureteric tip (Fig. S3B). To investigate whether UE clustering requires homophilic cadherin interactions, dissociations and subsequent reaggregation cultures were performed in the presence of blocking antibodies to either E-cadherin or P-cadherin. Immunofluorescence analyses were performed at 8 and 24 h to analyse cytokeratin$^+$ UE cluster size

Development (2017) 144, 1087-1096 doi:10.1242/dev.140228

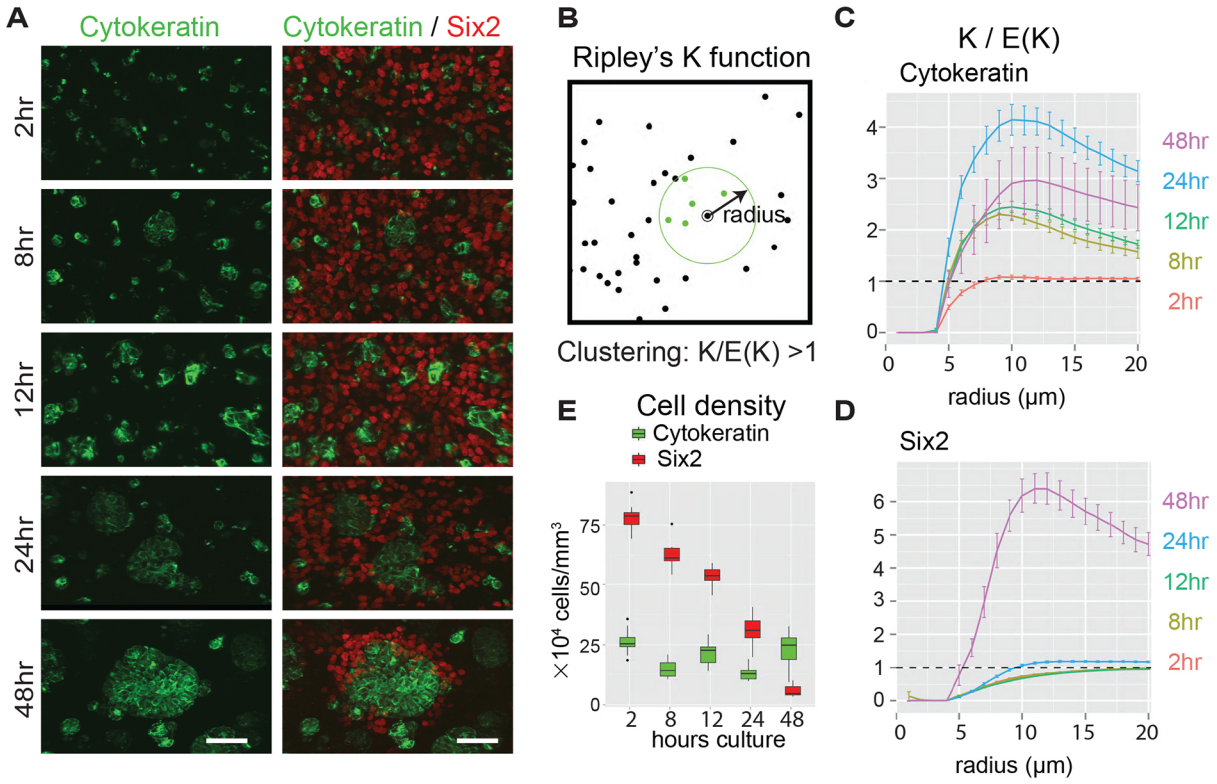

Fig. 3. Self-organisation commences with clustering of ureteric epithelial cells. (A) Sample images showing the relative localisation of UE and CM cells across a 48 h reaggregation culture timecourse. With time, progressive clustering of UE cells (cytokeratin$^+$; green) is seen within the field of CM cells (Six2$^+$; red). Scale bars: 30 µm. (B) The Ripley's *K* function (Hansson et al., 2013) is a general multi-scale clustering metric. For a specified radius *r*, *K*(*r*) is the average number of cells within distance *r* of a given reference cell, divided by the overall cell density (see Fig. S2B,C). *K*(*r*) was calculated separately for cytokeratin$^+$ and Six2$^+$ cells at each culture period, for integer radius values from 1 to 20 µm. (C,D) Plots of Ripley's *K* divided by the expected value under random distribution [*K*/*E*(*K*)] (mean±s.e.m. of image sections). Values >1 indicate clustering. Values <1 are seen at radii less than ∼5 µm, owing to physical exclusion (cells cannot occupy the same space). (C) Substantial clustering is seen in the UE cells by 8 h, and progresses steadily until 24 h. (D) Clustering in CM cells is not seen until 24 h, but increases greatly over the following 24 h. (E) Six2$^+$ and cytokeratin$^+$ cell density (cells per unit volume) by image section (Tukey boxplot). Six2 cell counts decrease steadily, suggesting progressive cell loss.

distributions (Fig. 5A,B). At 8 h, the modal cluster size was reduced in the presence of cadherin-blocking antibodies compared with control cultures (Fig. 5B; Fig. S3C), with anti-P-cadherin preincubation causing the most significant reduction in cluster size (Fig. S3C). Ripley's *K* analyses did not show a robust difference in evidence for UE clustering at 24 h (Fig. S3C), hence clustering occurred but the size of clusters was reduced. Although the addition of anti-P-cadherin blocking antibody seemed to reduce overall cell density in some experiments, this was not reproducible, whereas the increase in unclustered cells was always apparent (Fig. S3D).

Upon cluster formation, cytokeratin$^+$ cells became polarised, as evidenced by the apical relocation of Pkcδ (also known as Prkcd), began to produce a laminin-containing basement membrane and formed a single lumen (Fig. 1E,F). An analysis of wild-type reaggregations showed an increase in apical polarisation, as assessed by the percentage of clusters with apical Pkcδ, with both time and cluster size. However, even some small clusters showed evidence of polarisation (Fig. 5C,E). At 8 h, laminin was present within the reaggregations both around and between UE clusters, but by 24 h this was distinct only around the basement membrane of both UE clusters and forming nephrons (Fig. 5G). A similar analysis of epithelial maturation after inhibition with anti-P-cadherin blocking antibodies, although confirming a delay in clustering at 8 h, showed evidence of recovery by 24 h and no apparent effect on the maturation of those clusters that do form (Fig. 5D,F,H). This suggests that although blocking of P-cadherin-mediated cell-cell adhesion disrupts the initiation of self-organisation, once cells have clustered, there is no long-term effect on maturation.

DISCUSSION

In this study, we have investigated the way in which the component cells from embryonic mouse kidney can reform structure after complete dissociation. This process of self-organisation seems to involve initial random cell motion coupled with adhesion-based self-association between cells of the UE. The recreation of nephron-forming niches comprising CM around an UE tip was seen to be a secondary event.

The population apparently driving reorganisation in such cultures is the UE. Quantitative analysis of cell movement and cell clustering across time, coupled with simulation modelling, suggests selective adhesion between UE cells is sufficient for the observed temporospatial patterning to arise. Disruption of P-cadherin-based interactions between UE cells delayed the process of UE clustering, but not of UE epithelial maturation. Although this suggests a role for P-cadherin in UE cell-cell interaction, it is difficult to determine the degree to which the addition of inactivating antibodies blocked homophilic interactions and hence how important this molecule is for normal ureteric morphogenesis *in vivo*. Indeed, Radice et al. (1997) report that P-cadherin knockout mice are viable and fertile; however, they did not examine kidney structure or function. Although blocking cadherins can clearly interrupt the rate of UE cell-cell interactions, within the cell, classical cadherins associate

Development (2017) 144, 1087-1096 doi:10.1242/dev.140228

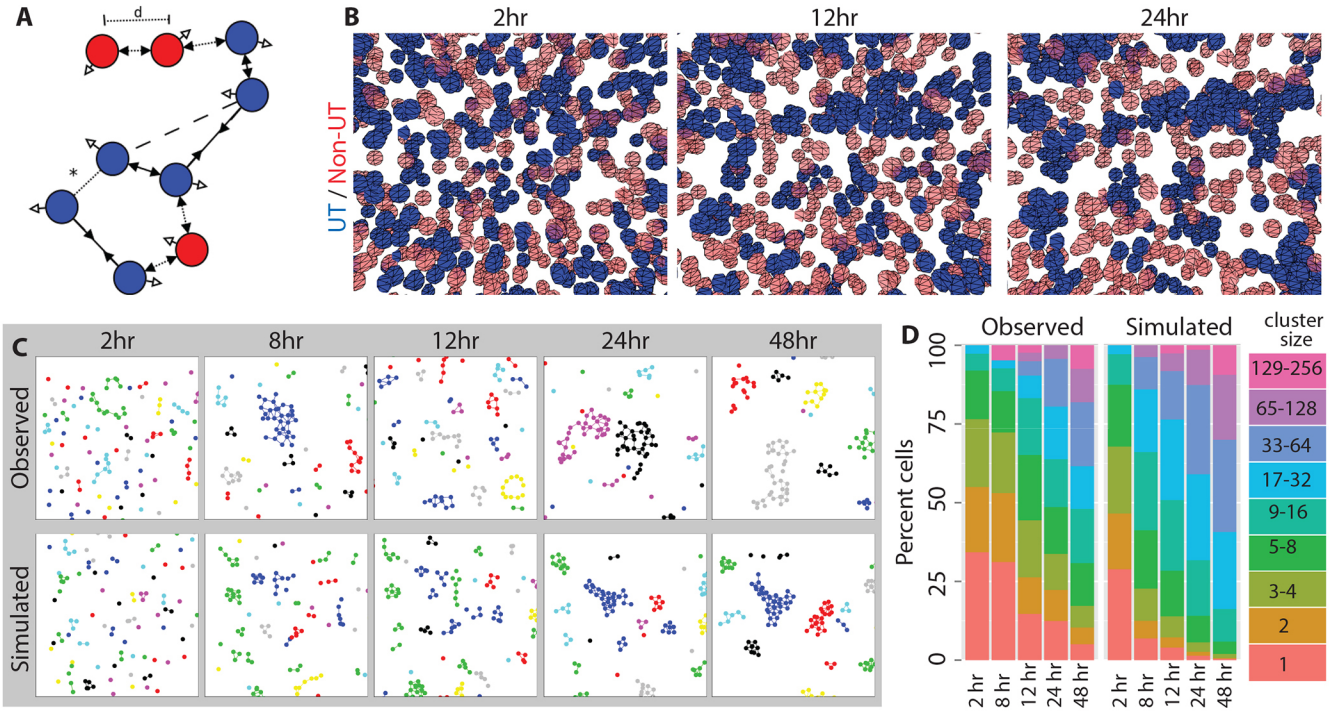

Fig. 4. Simulation of cell clustering via random motion and differential cell-cell adhesion predicts observed behaviour. (A) Illustration of a model showing ureteric (blue) and non-ureteric (red) cells, adhesion bonds (solid lines) between ureteric cells and three forces (arrows). Forces include (1) repulsion between cells with diameter (d)<8 µm (filled arrowhead, divergent); (2) attraction between cells with an adhesion bond and d>8 µm (filled arrowhead, convergent) and (3) random force on each cell modelling Brownian motion (unfilled arrowhead). Cell positions are iteratively updated based on the net force acting at each time step. Adhesion bonds are added probabilistically between ureteric cells with d<10 µm (*) and removed if d>12 µm (dashed line). If an adhesion bond is added at *, the two clusters depicted will merge. See Fig. S2D-F and supplementary Materials and Methods for full specification and calibration to experimental data. (B) Screenshot of simulation section at 2 h, 8 h and 24 h showing ureteric (blue) and non-ureteric (red) cells. Lines joining ureteric cells indicate adhesion bonds. (C) 2D projection of observed and simulated ureteric cell distribution, 2-48 h, randomly sampled 200×200×15 µm sections. Colours indicate clusters. In real data, adhesion bonds are imputed between pairs of UE cells within 12 µm. (D) Distribution of ureteric epithelial cluster sizes by culture time, showing a similar progression of clustering to the simulation.

with the actin cytoskeleton and recruit catenins as well as other effectors of cell signalling and modulators of cell structure. Cadherins can also act as mechano- or tension sensors (Niessen et al., 2011). These subsequent consequences of successful cadherin signalling could prove more important to self-organisation than simple adhesion, as has been recently proposed (Shi et al., 2008; Gomez et al., 2011). What is clear is that the CM will associate with the UE even though the cluster sizes are smaller (Fig. S3E,F). The mechanism for CM clustering in this pattern remains to be investigated. Although one might assume the CM responds to UE-produced factors, possibly via chemotaxis, or differential survival or proliferation, this might also require differential cell adhesion between these cells of distinct identity.

The power of organotypic self-organisation has been recently illustrated by means of the formation of organoids representative of a number of different tissue types, including the kidney (Takasato and Little, 2015), from human pluripotent stem cells. Although the embryonic kidney is not normally faced with this challenge, the fact that such structures can reform suggests a role for such cell-cell interactions in maintaining structure *in vivo*. From the perspective of recreating such tissues *in vitro*, this advance in understanding provides an opportunity to guide or manipulate structure.

One of the major challenges of kidney organoids derived from human pluripotent stem cells is the absence of a single unified collecting duct network with an exiting ureter. This was highlighted in commentary in response to the recent publication of kidney organoids (Davies, 2015). Indeed, a modified approach to embryonic kidney reaggreations has been to isolate intact ureteric epithelial trees and co-culture with dissociated embryonic kidney (Ganeva et al., 2011). Future bioengineering approaches might not be able to benefit from nucleation around an existing UE and might have to rely upon the additive bioprinting of cells together with innate cellular properties of self-organisation (Ilagan et al., 2015). In either instance, what we demonstrate here suggests that the promotion of P-cadherin-based UE cluster formation, as well as balancing of the relative numbers of non-UE versus UE cells within organoids, might allow for the appropriate positioning of UE within bioengineered structures. Overall, understanding the driving forces present during self-organisation brings the prospect of enhanced tissue bioengineering approaches to facilitate the recreation of a more architecturally accurate model of this complex organ.

MATERIALS AND METHODS

Animals

All animal experimentation was performed in accordance with the Australian code for the care and use of animals for scientific purposes 8th edition (2013), and with approval from a University of Queensland Animal Ethics Committee. Animals used included outbred CD1 mice and Six2TGC:TdTomato:Hoxb7GFP triple transgenic mice in which the CM is labelled green and red while the *Six2* promoter is active and red thereafter, whereas the UE is green as long as the *Hoxb7* promoter is active.

Reaggregation cultures

Reaggregation cultures were performed as previously described (Unbekandt and Davies, 2010; Lusis et al., 2010; Hendry et al., 2013). In a modified

Development (2017) 144, 1087-1096 doi:10.1242/dev.140228

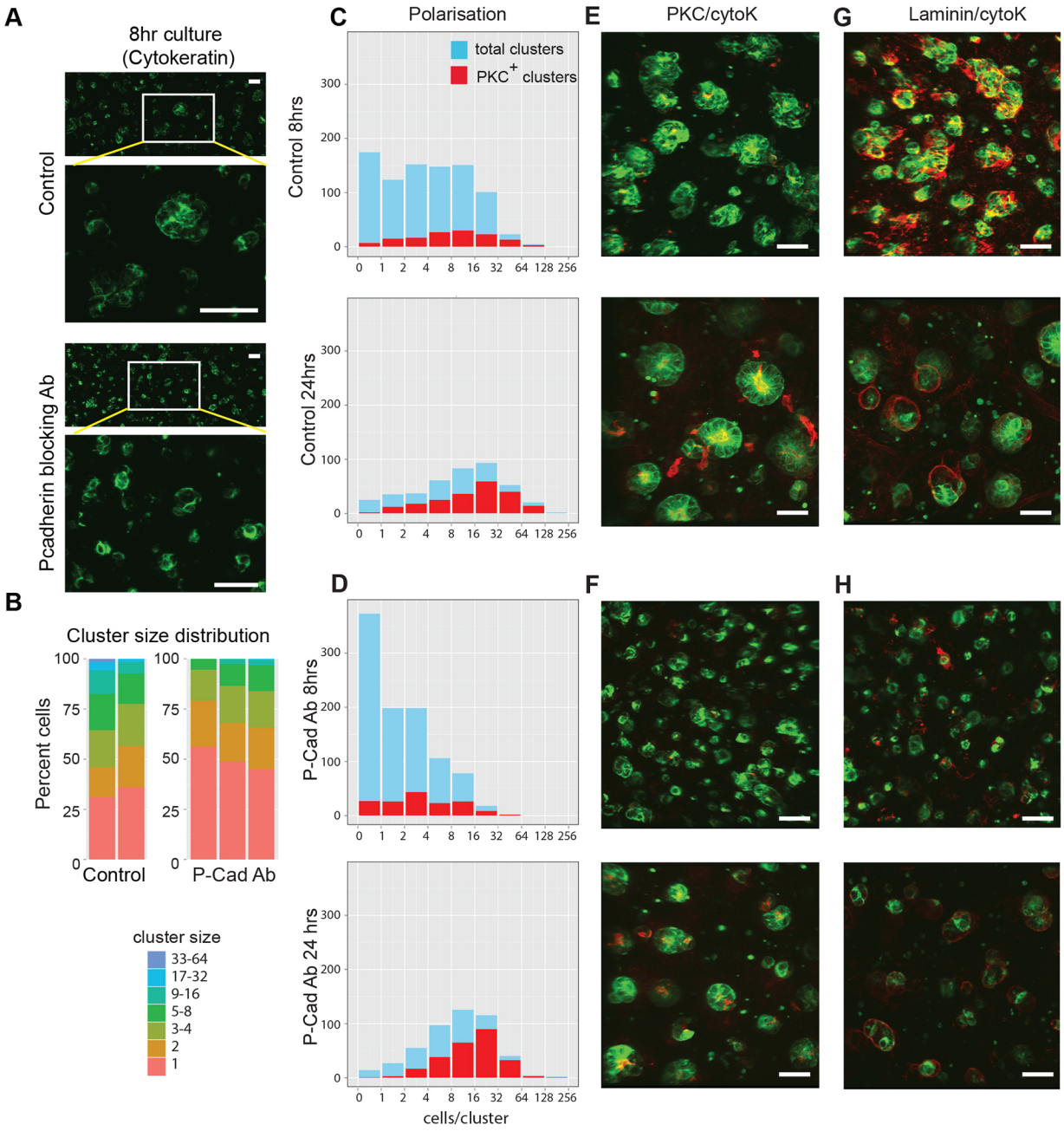

Fig. 5. P-cadherin blocking affects initial clustering without preventing epithelial maturation. (A) High and low magnification immunofluorescence images of control and anti-P-cadherin-treated aggregation cultures illustrating a reduction in UE cluster size after P-cadherin blocking. (B) Distribution of cluster sizes also shows reduced clustering associated with P-cadherin inhibition. (P=0.0086 by Kruskal-Wallis stratified rank sum test). (C-H) Analysis of UE maturation in control and anti-P-cadherin-treated cultures at 8 and 24 h after reaggregation. (C,D) Number of total clusters and number of apical Pkcδ$^+$ clusters of each indicated size band in control (C) and anti-P-cadherin-treated (P-cad; D) reaggregations at 8 and 24 h. Pkcδ marks the apical surface of polarised epithelium (Durgan et al., 2011). (E,F) Images of UE clusters at 8 and 24 h post reaggregation in control (E) and anti-P-cadherin-treated (F) cultures showing UE (cytokeratin$^+$; green) and apical Pkcδ (red). (G,H) Images of UE clusters at 8 and 24 h post reaggregation in control (G) and anti-P-cadherin-treated (H) cultures showing laminin$^+$ basement membrane formation; UE (cytokeratin$^+$; green) and basement membrane (laminin$^+$; red). Scale bars: 30 µm.

version of these prior protocols, murine embryonic kidneys were harvested at 13.0 dpc, manually minced then dissociated to a single-cell suspension with Accutase (Life Technologies). Each aggregate, comprising 4×10^5 centrifuged single cells, was cultured on a Transwell membrane insert (Sigma) in a 6-well plate containing 700 µl of DMEM (Life Technologies) plus 10% foetal bovine serum (Scientifix), and 1% penicillin-streptomycin (Life Technologies). Unlike previously reported protocols (Davies et al., 2012), aggregates were not cultured in the presence of ROCKi (designed to reduce cell death) or on a monolayer of Wnt-expressing NIH3T3 (Lusis et al., 2010). We did not find that either of these features was required when commencing with 13.0 dpc embryonic kidneys. Aggregates were simply plated directly onto Transwell filters at a fixed cell number (Fig. 1B; Fig. S2A). To block cadherin-cadherin interactions, single-cell suspensions were incubated in the recommended maximal inhibiting concentration of blocking antibody (50 µg/ml for anti-P-cadherin, 10 µg/ml for DECMA-1) for 30 min at 37°C before centrifugation. Blocking antibodies were also added at the same concentration to the culture medium. All aggregates were cultured from 2 to 48 h before fixation with 4% paraformaldehyde.

Development (2017) 144, 1087-1096 doi:10.1242/dev.140228

Immunofluorescence and imaging

Antibodies used included anti-Six2 (Proteintech, #11562-1-AP), anti-cytokeratin (Abcam, #Ab115959), anti-GFP (Abcam, #Ab13970), anti-RFP (MBL International, #PM005), anti-PKCζ (Santa Cruz, #SC-216), anti-laminin (Sigma-Aldrich, #L9393), anti-CDH3/P-cadherin (Sapphire Bioscience, #LS-C150227), anti-E-cadherin/DECMA-1 (Abcam, #Ab11512); and Alexa Fluor 488 goat anti-mouse IgG (H+L) and Alexa Fluor 568 goat anti-rabbit IgG (H+L) secondary antibodies (Life Technologies, #A11001 and #A11011). All antibody staining was performed as previously described (Davies et al., 2012). In brief, the 4% paraformaldehyde-fixed and PBS-washed aggregates were excised from the Transwell membrane filter individually with a scalpel and forceps. The aggregates were blocked for 2 to 4 h at room temperature in a glass-bottom dish (MatTEK, #P35G-0-14-C) containing 150 µl of blocking buffer [10% fetal bovine serum in PBTX (PBS+0.1% Triton X-100)]. After incubation, the blocking buffer was removed and replaced with the desired primary antibody combination at a dilution of 1:400 overnight at 4°C. Primary antibody was removed from the glass-bottom dishes and aggregates were washed with PBS and Triton X-100 six times at 10 min intervals. The aggregates were incubated with the secondary antibody for 6 h followed by 30 min of DAPI (Sigma-Aldrich) staining. DAPI was then removed and aggregates were washed with PBS three times for 10 min each prior to imaging. Each aggregate was placed in the glass-bottom dish with just enough PBS to keep the aggregate submerged. Each aggregate was imaged using the Zeiss LSM-510 confocal microscope with a 40× oil-immersion objective. A 3×1 tiled z-stack image was scanned from top to bottom of the aggregate with each imaging region being: x=675 µm, y=225 µm and z=30-50 µm (Fig. S2A). Optical sections were 2.1 µm thick and spaced at 6.35 µm intervals to ensure that a substantial region of each sample was represented by consecutive, but non-overlapping, sections. Using Imaris version 7.2 (Bitplane), the number and position of nuclei within a cluster was determined by creating a surface rendering that defined 3D volumes occupied by fluorescent signal from the cytokeratin staining. This surface was used to isolate DAPI signal within the volumes defined by the cytokeratin staining. The Imaris spot-counting algorithm was then used to determine the number and position (in x, y, and z) of nuclei within these regions (Fig. S2B), which was used for 3D Ripley's K analysis (Fig. S2C).

Live imaging was performed on samples grown on a suspended filter in a glass-bottom dish in a humidified chamber heated to 37°C and supplemented with 5% CO_2 (Costantini et al., 2011). For Fig. 1C, an inverted Olympus IX-81 OBS microscope was used to take brightfield images every 5 min for 23 h at 10× magnification. The sample was then imaged using confocal reflection microscopy at 10× to reveal internal epithelial structures. For Fig. 2, an inverted Zeiss LSM 710 confocal was used to take images every 8 min for ∼7 h hours at 40× magnification. Five optical sections of 5.91 µm gave data from a z range of 23.64 µm. These imaging settings were optimised to minimise phototoxicity while retaining a capacity to track cell movement.

Live imaging quantification

The Imaris particle-tracking tool was used to identify cell tracks (series of spots over time) by temporospatial matching. Tracks that branched due to mitosis were divided into unbranched sections for motility analysis. The finite difference $v(c,\ t)=(v_x(c,\ t),\ v_y(c,\ t))=(x(c,\ t)-x(c,\ t-1),\ y(c,\ t)-y(c,\ t-1))$ was used to approximate the velocity of cell c at time step t; the z-position data were excluded due to lower resolution. These values were calculated wherever the position of cell c is available at consecutive time points, and used to obtain the velocity variance:

$$s^2 = \overline{\boldsymbol{v}(c,t) - \overline{\boldsymbol{v}(c,t)}^2},$$

and autocorrelation

$$R(\tau) = \overline{(\boldsymbol{v}(c,t) - \bar{\boldsymbol{v}}(c,t)) \cdot (\boldsymbol{v}(c,t-\tau) - \overline{\boldsymbol{v}(c,t)})}/s^2,$$

where the bar denotes the mean over all cells c and time steps t for which values are available.

Quantification of clustering

Two approaches were used to quantify clustering in observed and simulated data: (1) Ripley's K in three dimensions; and (2) the distribution of cluster sizes. In all cases we worked from a specified set of cell nuclei [primarily ureteric (cytokeratin$^+$) cells, although Ripley's K was also calculated for the CM (Six2$^+$) cells] within a defined volume, each cell represented by its centre position.

Ripley's K function is a widely used metric for quantifying clustering over a range of distance scales. For a given radius r, $K(r)$ is an estimate of the expected number of cells within distance r of a randomly selected reference cell, divided by overall cell density (the count does not include the reference cell). Calculations were performed in 3D using the RipleyGUI module for MATLAB (MathWorks).

In contrast to the Ripley's K function, analysis of the cluster size distribution requires identification of cell clusters. This was done on experimental data using a threshold distance within which two cells were assumed to belong to the same cluster. The threshold was calibrated against the experimental timecourse data, by considering the distribution of nearest neighbour distances (the distance from each cytokeratin$^+$ cell to the nearest other cytokeratin$^+$ cell, see Fig. S2D). A threshold of 12 µm was chosen. The threshold was verified by inspection of identified clusters (see, for example, Fig. 4C), although this is less clear at early stages (particularly 2 h). For simulated data, cluster information is included in the output, as the model incorporates adhesion bonds (see below).

Ripley's K has the advantage of depending on cell positions only, providing the most objective measure of whether clustering is present. In contrast, there is some degree of ambiguity in the delineation of clusters in experimental data, which is more pronounced where the existence of clustering is uncertain. However, the distribution of cluster sizes provides a more biologically meaningful characterisation, where Ripley's K might be hard to interpret.

Both approaches are potentially sensitive to variation in the cell density, whether it is a difference in the total number of cells per unit volume or the proportion of cells that are in the population of interest. Higher density can be expected to result in more or larger clusters, for any plausible clustering mechanism. The effect on Ripley's K is less clear; the value is adjusted for density, but this will not necessarily account for the potentially non-linear effect of density on the biological clustering mechanism. Interpretation of results must consider this potential confounder.

Simulation of clustering behaviour

Cell culture simulations were performed with software written in the Processing 2 programming language (https://processing.org/). The code has been placed online under a free licence (https://github.com/jameslefevre/self-organisation-simulation). A description of the model specification and simulation calibration is described in supplementary Materials and Methods.

Statistics

Multiple sections were imaged from each reaggregation sample (Fig. S2A), and clustering metrics (Ripley's K and cluster size distribution) were calculated for each image section. For the timecourse data, an ANOVA performed on Ripley's K values at 10 µm for each culture period found no evidence for heterogeneity between samples (P>0.05), so image section data were pooled across explants for s.e.m. calculation (Fig. 3C). Image/explant counts were 12/2 (2 h), 9/2 (8 h), 13/3 (12 h), 12/3 (24 h), 7/2 (48 h). However, heterogeneity between explants was evident in the cadherin experiments, and hence analysis used explant means. Evidence for reduced clustering in anti-P-cadherin-treated cultures at 8 h was assessed using the Kruskal–Wallis stratified rank sum test (stratified Wilcoxon), to pool three heterogeneous experiments, giving P=0.0086, or P=0.034 excluding the original (exploratory) experiment. The image/explant counts were 5/2, 3/1, 6/2 for controls and 5/2, 6/2, 8/3 for treatment. The first repeat also included two explants (six images) treated with DECMA (Fig. S3C). Fig. 5B shows the third repeat. To control for cell density as a possible confounder, tests were performed on both Ripley's K at 10 µm and median cell cluster size, which showed opposing response to density variation, and we also performed multivariate linear regressions for each metric and each of the

Development (2017) 144, 1087-1096 doi:10.1242/dev.140228

confirmation experiments, on image section level data with sample and density included as independent variables (P<0.011 across the four cases). For Fig. 5C,D, two explants were used for each of the four treatment groups.

Acknowledgements

We acknowledge the Australian Cancer Research Foundation for support of the IMB Imaging facility and thank Rob Parton and Katharina Gaus for discussions around Ripley's *K* analyses. MCRI is supported by the State Government of Victoria Operational Infrastructure Support Program.

Competing interests

The authors declare no competing or financial interests.

Author contributions

J.G.L.: Design, analysis, interpretation, collation and presentation of the data, and substantial writing of the manuscript, primary contributor of mathematical and statistical analysis and modelling of cell aggregation. H.S.C.: Performed aggregation assays, imaging and Imaris-based analysis, design, analysis, interpretation, collation and presentation of the data, and writing of the manuscript. A.N.C. and J.M.V.: Experimental design, supervision and interpretation. A.N.C.: Advised on imaging, data presentation and interpretation. A.J.: Technical assistance with cell aggregation cultures and their imaging. N.A.H.: Supervised and contributed to mathematical modelling, statistical analysis, data presentation and interpretation and writing the manuscript. M.H.L.: Conceived and supervised the project, designed experiments, contributed to data analysis, interpretation and presentation and performed the primary role in design of the study and played a major role in manuscript writing. All authors contributed to editing the manuscript.

Funding

M.H.L. is a Senior Principal Research Fellow of the National Health and Medical Research Council (APP1042093). A.N.C. is an Australian Research Council DECRA Postdoctoral Fellow (DE150100652). This work was supported by the Australian Research Council (DP130102939) and the National Health and Medical Research Council (APP1063989).

Data availability

The code for simulation of clustering behaviour has been deposited in GitHub (https://github.com/jameslefevre/self-organisation-simulation).

Supplementary information

Supplementary information available online at
http://dev.biologists.org/lookup/doi/10.1242/dev.140228.supplemental

References

Ader, M. and Tanaka, E. M. (2014). Modeling human development in 3D culture. *Curr. Opin. Cell Biol.* **31**, 23-28.

Barak, H., Huh, S.-H., Chen, S., Jeanpierre, C., Martinovic, J. Parisot, M., Bole-Feysot, C., Nitschké, P., Salomon, R., Antignac, C. et al. (2012). FGF9 and FGF20 maintain the stemness of nephron progenitors in mice and man. *Dev. Cell* **22**, 1191-1207.

Bonner, J. T. (1947). Evidence for the formation of cell aggregates by chemotaxis in the development of the slime mould Dictyostelium discoideum. *J. Exp. Zool.* **106**, 1-26.

Boyle, S., Misfeldt, A., Chandler, K. J., Deal, K. K., Southard-Smith, E. M., Mortlock, D. P., Baldwin, H. S. and de Caestecker, M. (2008). Fate mapping using Cited1-CreERT2 mice demonstrates that the cap mesenchyme contains self-renewing progenitor cells and gives rise exclusively to nephronic epithelia. *Dev. Biol.* **313**, 234-245.

Carroll, T. J., Park, J.-S., Hayashi, S., Majumdar, A. and McMahon, A. P. (2005). Wnt9b plays a central role in the regulation of mesenchymal to epithelial transitions underlying organogenesis of the mammalian urogenital system. *Dev. Cell* **9**, 283-292.

Combes, A. N., Davies, J. A. and Little, M. H. (2015). Cell-cell interactions driving kidney morphogenesis. In: cellular adhesion in development and disease. *Curr. Top. Dev. Biol.* **112**, 467-508.

Costantini, F., Watanabe, T., Lu, B., Chi, X., Srinivas, S. (2011) Dissection of embryonic mouse kidney, culture in vitro, and imaging of the developing organ. *Cold Spring Harb. Protoc.* **2011**, pdb.prot5613.

Davies, J. A. (2015). Biological techniques: kidney tissue grown from induced stem cells. *Nature* **526**, 512-513.

Davies, J. A., Unbekandt, M., Ineson, J., Lusis, M. and Little, M. H. (2012). Dissociation of embryonic kidney followed by re-aggregation as a method for chimeric analysis. *Methods Mol. Biol.* **886**, 135-146.

Durgan, J., Kaji, N., Jin, D. and Hall, A. (2011). Par6B and atypical PKC regulate mitotic spindle orientation during epithelial morphogenesis. *J. Biol. Chem.* **286**, 12461-12474.

Eiraku, M., Takata, N., Ishibashi, H., Kawada, M., Sakakura, E., Okuda, S., Sekiguchi, K., Adachi, T. and Sasai, Y. (2011). Self-organising optic-cup morphogenesis in three-dimensional culture. *Nature* **242**, 51-56.

Foty, R. A., Pfleger, C. M., Forgacs, G. and Steinberg, M. S. (1996). Surface tensions of embryonic tissues predict their mutual envelopment behavior. *Development* **122**, 1611-1620.

Ganeva, V., Unbekandt, M. and Davies, J. A. (2011). An improved kidney dissociation and reaggregation culture system results in nephrons arranged organotypically around a single collecting duct system. *Organogenesis* **7**, 83-87.

Georgas, K., Rumballe, B., Valerius, M. T., Chiu, H. S., Thiagarajan, R. D., Lesieur, E., Aronow, B. J., Brunskill, E. W., Combes, A. N., Tang, D. et al. (2009). Analysis of early nephron patterning reveals a role for distal RV proliferation in fusion to the ureteric tip via a cap mesenchyme-derived connecting segment. *Dev. Biol.* **332**, 273-286.

Gomez, G. A., McLachlan, R. W. and Yap, A. S. (2011). Productive tension: force-sensing and homeostasis of cell-cell junctions. *Trends Cell Biol.* **21**, 499-505.

Grover, J. W. (1963). Reaggregation and organotypic redevelopment of dissociated embryonic chick lung cells in short-term culture. *Natl. Cancer Inst. Monogr.* **11**, 35-50.

Hansson, K., Jafari-Mamaghani, M. and Krieger, P. (2013). RipleyGUI: software for analyzing spatial patterns in 3D cell distributions. *Front. Neuroinform.* **7**, 5.

Harding, S. D., Armit, C., Armstrong, J., Brennan, J., Cheng, Y., Haggarty, B., Houghton, D., Lloyd-MacGilp, S., Pi, X., Roochun, Y. et al. (2011). The GUDMAP database–an online resource for genitourinary research. *Development* **138**, 2845-2853.

Hendry, C., Rumballe, B. A., Moritz, K. and Little, M. H. (2011). Defining and redefining the nephron progenitor population. *Pediatr. Nephrol.* **26**, 1395-1406.

Hendry, C. E., Vanslambrouck, J. M., Ineson, J., Suhaimi, N., Takasato, M., Rae, F. and Little, M. H. (2013). Direct transcriptional reprogramming of adult cells to embryonic nephron progenitors. *J. Am. Soc. Nephrol.* **24**, 1424-1434.

Holtfreter, J. (1939). Gewebeaffinitat, ein Mittel der embryolnalen Formbilding. *Arch. Exp. Zellforsch.* **23**, 169.

Holtfreter, J. (1943). A study of the mechanics of gastrulation. *J. Exp. Zool.* **94**, 261.

Ilagan, R., Rapoport, S., Shepherd, B. and Presnell, S. (2015). Tissue engineering through additive manufacturing: hope for a bioengineered kidney? In *Kidney Development, Disease, Repair and Regeneration* (ed. M. H. Little), pp. 555-568. Academic Press.

Karner, C. M., Das, A., Ma, Z., Self, M., Chen, C., Lum, L., Oliver, G. and Carroll, T. J. (2011). Canonical Wnt9b signaling balances progenitor cell expansion and differentiation during kidney development. *Development* **138**, 1247-1257.

Kobayashi, A., Valerius, M. T., Mugford, J. W., Carroll, T. J., Self, M., Oliver, G. and McMahon, A. P. (2008). Six2 defines and regulates a multipotent self-renewing nephron progenitor population throughout mammalian kidney development. *Cell Stem Cell* **3**, 169-181.

Lancaster, M. A., Renner, M., Martin, C. A., Wenzel, D., Bicknell, L. S., Hurles, M. E., Homfray, T., Penninger, J. M., Jackson, A. P. and Knoblich, J. A. (2013). Cerebral organoids model human brain development and microcephaly. *Nature* **501**, 373-379.

Little, M. H. and McMahon, A. P. (2012). Mammalian kidney development: principles, progress, and projections. *Cold Spring Harb. Perspect. Biol.* **4**.

Lusis, M., Li, J., Ineson, J., Christensen, M. E., Rice, A. and Little, M. H. (2010). Isolation of clonogenic, long-term self-renewing embryonic renal stem cells. *Stem Cell Res.* **5**, 23-39.

McCracken, K. W., Catá, E. M., Crawford, C. M., Sinagoga, K. L., Schumacher, M., Rockich, B. E., Tsai, Y. H., Mayhew, C. N., Spence, J. R., Zavros, Y. et al. (2014). Modelling human development and disease in pluripotent stem-cell-derived gastric organoids. *Nature* **516**, 400-404.

Niessen, C. M., Leckband, D. and Yap, A. S. (2011). Tissue organization by cadherin adhesion molecules: dynamic molecular and cellular mechanisms of morphogenetic regulation. *Physiol. Rev.* **91**, 691-731.

Radice, G. L., Ferreira-Cornwell, M. C., Robinson, S. D., Rayburn, H., Chodosh, L. A., Takeichi, M. and Hynes, R. O. (1997). Precocious mammary gland development in P-cadherin-deficient mice. *J. Cell Biol.* **139**, 1025-1032.

Shi, Q., Chien, Y. H. and Leckband, D. (2008). Biophysical properties of cadherin bonds do not predict cell sorting. *J. Biol. Chem.* **283**, 28454-28463.

Short, K. M., Combes, A. N., Lefevre, J., Ju, A. L., Georgas, K. M., Lamberton, T., Cairncross, O., Rumballe, B. A., McMahon, A. P., Hamilton, N. A. et al. (2014). Global quantification of tissue dynamics in the developing mouse kidney. *Dev. Cell* **29**, 188-202.

Spence, J. R., Mayhew, C. N., Rankin, S. A., Kuhar, M. F., Vallance, J. E., Tolle, K., Hoskins, E. E., Kalinichenko, V. V., Wells, S. I., Zorn, A. M. et al. JM. (2011). Directed differentiation of human pluripotent stem cells into intestinal tissue in vitro. *Nature* **470**, 105-109.

Srinivas, S., Goldberg, M. R., Watanabe, T., D'Agati, V., al-Awqati, Q. and Costantini, F. (1999). Expression of green fluorescent protein in the ureteric bud of transgenic mice: a new tool for the analysis of ureteric bud morphogenesis. *Dev. Genet.* **24**, 241-251.

Development (2017) 144, 1087-1096 doi:10.1242/dev.140228

Steinberg, M. S. (1962). On the mechanism of tissue reconstruction by dissociated cells, III. Free energy relations and the reorganization of fused, heternomic tissue fragments. *Proc. Natl. Acad. Sci. USA* **48**, 1769-1776.

Steinberg, M. S. (1970). Does differential adhesion govern self-assembly processes in histogenesis? Equilibrium configurations and the emergence of a hierarchy among populations of embryonic cells. *J. Exp. Zool.* **173**, 395-433.

Steinberg, M. S. and Takeichi, M. (1994). Experimental specification of cell sorting, tissue spreading, and specific spatial patterning by quantitative differences in cadherin expression. *Proc. Natl. Acad. Sci. USA* **91**, 206-209.

Suga, H., Kadoshima, T., Minaguchi, M., Ohgushi, M., Soen, M., Nakano, T., Takata, N., Wataya, T., Muguruma, K., Miyoshi, H. et al. (2011). Self-formation of functional adeno-hypophysis in three-dimensional culture. *Nature* **480**, 57-62.

Takasato, M. and Little, M. H. (2015). Generating a self-organising kidney from pluripotent cells. *Curr. Opin. Organ Transpl.* **20**, 178-186.

Takasato, M., Osafune, K., Matsumoto, Y., Kataoka, Y., Yoshida, N., Meguro, H., Aburatani, H., Asashima, M. and Nishinakamura, R. (2004). Identification of kidney mesenchymal genes by a combination of microarray analysis and Sall1-GFP knockin mice. *Mech. Dev.* **121**, 547-557.

Takasato, M., Er, P. X., Chiu, H. S., Maier, B., Baillie, G. J., Ferguson, C., Parton, R. G., Wolvetang, E. J., Roost, M. S., Lopes, S. M. et al. (2015). Kidney organoids from human iPS cells contain multiple lineages and model human nephrogenesis. *Nature* **526**, 564-568.

Trinkaus, J. P. and Groves, P. W. (1955). Differentiation in culture of mixed aggregates of dissociated tissue cells. *Proc. Natl. Acad. Sci. USA* **41**, 787-795.

Unbekandt, M. and Davies, J. A. (2010). Dissociation of embryonic kidneys followed by reaggregation allows the formation of renal tissues. *Kidney Int.* **77**, 407-416.

Weiss, P. and Taylor, A. C. (1960). Reconstitution of complete organs from single-cell suspensions of chick embryos in advanced stages of differentiation. *Proc. Natl. Acad. Sci. USA* **46**, 1177-1185.

Wilson, H. V. (1907). On some phenomena of coalescence and regeneration in sponges. *J. Exp. Zool.* **5**, 245-258.

Supplementary Materials and Methods

The reaggregation simulation model consists of a set of ureteric and non-ureteric cells represented as points in a three dimension rectangular volume, with adhesions between certain pairs of ureteric cells. Cells are initially placed at random. At each subsequent time point, positions are updated based on repulsive impulses between pairs of nearby cells and attractive impulses between pair of ureteric cells connected by an adhesion, plus a random impulse at each cell. At each time step, prior to the calculation of these impulses, the adhesion relationships are updated by removing any adhesions between cells separated by more than a threshold distance, and adding, with a certain probability, an adhesion between each pair of ureteric cells which are separated by less than a second (smaller) threshold distance but do not currently have an adhesion relationship. After cell positions have been updated based on the calculated impulses, positions beyond the defined volume are reverted to the nearest boundary point, in order to maintain a known cell density.

Note that physical momentum is not included in the model. It is assumed that the external forces acting on a cell rapidly reach equilibrium with drag, and hence cell velocity at any time can be well approximated as a function of the instantaneous forces acting on the cell.

Model specification

The simulation parameters are specified in the following table, with corresponding variable names used in the code implementing the algorithm.

parameter	variable name	description	Value
σ_{sim}	brownianMotionPerTimestepStdev	The standard deviation of the random displacement added to each dimension of the position of each cell at each time step.	0.2
n	type1cells + type2cells	Total number of cells	6800 / 13600
m	type2cells	Number of ureteric cells	6800
X, Y, Z	xDim,yDim,zDim	Define 3D volume in which the simulation takes place	680,250,200
d_r	cellSpacingForceDist	Repulsion force applied to cells closer than this distance, modelling physical exclusion	8
f_r	cellSpacingForceStrength	Repulsion force is proportional to this value	0.8
d_a^c	createAdhesionDist	Adhesion bonds may be formed between cells within this distance of each other.	10
p_a	adhesionFormationProbability	If they are close enough to form an adhesion bond, this is the probability of a bond being created each time step.	0.005
d_a^b	breakAdhesionDist	Adhesion bonds between cells further apart than this are removed	12

d_a	adhesionSpringLength	If there is an adhesion bond between two cells but they are greater than this distance, an attractive force is applied	8
f_a	adhesionSpringForce	Adhesion force is proportional to this value	0.02

The model representation at time point $t \in \mathbb{Z}^+ \cup \{0\}$ consists of a set of n cell positions $\boldsymbol{p_i}(t) \in \boldsymbol{V} = [0, X] \times [0, Y] \times [0, Z]$, for $i = 1, \ldots, n$, of which the first $m \leq n$ correspond to ureteric cells capable of adhering to each other, and a set $A(t) \subseteq \{(i, j): 1 \leq i < j \leq m\}$ representing adhesions between ureteric cell pairs.

Let $\mathcal{N}_i(t) = \{j: (i, j) \in A(t) \; or \; (j, i) \in A(t)\}$ represent the set of cells adhering to cell i at time t, and let $d_{ij}(t) = \|\boldsymbol{p}_i(t) - \boldsymbol{p}_j(t)\|$ and $\hat{\boldsymbol{p}}_{ij}(t) = \left(\boldsymbol{p}_i(t) - \boldsymbol{p}_j(t)\right)/d_{ij}(t)$. The model is initialised by generating n cell positions selected uniformly at random from the volume $\boldsymbol{V}$: $\boldsymbol{p_i}(0) \sim \mathcal{U}(0, X) \times \mathcal{U}(0, Y) \times \mathcal{U}(0, Z)$.

At time step $t \geq 1$, the model is updated as follows:

$A(t) = \{(i, j) \mid (i, j) \in A(t-1) \wedge d_{ij}(t) \leq d_a^b\} \cup \{(i, j) \mid 1 \leq i < j \leq m \wedge d_{ij}(t) \leq d_a^c \wedge \mathrm{I_{ijt}}\}$,

where I_{ijt} is a independent random boolean variable with $P(I_{ijt}) = p_a$;

$\boldsymbol{p}_i(t)' = \boldsymbol{p}_i(t-1) + \boldsymbol{F}_b(i, t) + \sum_{j \neq i} \boldsymbol{F}_r(i, j, t) + \sum_{j \in \mathcal{N}_i(t)} \boldsymbol{F}_a(i, j, t)$, where

$\boldsymbol{F}_r(i, j) = \max(d_{ij}(t-1) - d_r, 0) \cdot f_r \cdot \hat{\boldsymbol{p}}_{ij}(t-1)$,

$\boldsymbol{F}_a(i, j) = \min(d_{ij}(t-1) - d_a, 0) \cdot f_a \cdot \hat{\boldsymbol{p}}_{ij}(t-1)$,

$\boldsymbol{F}_b(i, t) \sim \mathcal{N}(0, {\sigma_{sim}}^2)^3$;

$$\boldsymbol{p}_i(t) = \begin{pmatrix} \max(0, \min(\boldsymbol{p}_{i1}(t)', X)) \\ \max(0, \min(\boldsymbol{p}_{i2}(t)', Y)) \\ \max(0, \min(\boldsymbol{p}_{i3}(t)', Z)) \end{pmatrix}$$

Simulation calibration

Simulation parameters were selected to match the experimental data in cell density (cells per unit volume), speed and separation between neighbouring cells.

Brownian motion (BM) is isotropic, with each component of motion independent, and thus the calibration calculations reduce to one dimension. Let $x(t)$ be the position of a cell at time point t along some arbitrary fixed axis, and $v(t) = x(t) - x(t-1)$. The velocity of a cell under BM is uncorrelated between successive time points, and can be characterised by a

diffusion constant $D = E((x(t+t_0) - x(t_0))^2)/t$. Live imaging analysis indicated significant positive autocorrelation between successive 15min time steps for Six2 cells, but motion over longer time scales that is consistent with BM for both Six2 and Hoxb7 cells (see Fig. 2). The observed single time-step displacement is modelled as $v(t) = f(t) + \lambda v(t-1)$, where $f(t) \sim \mathcal{N}(0, \sigma_f^2)$ is an independent random variable and λ is the autocorrelation between successive time steps. Then

$$(x(t+t_0) - x(t_0))^2 = \left[\sum_{i=1}^{t} v(i+v_0)\right]^2 = \sum_{i=1}^{t}\sum_{j=1}^{t} v_x(i+t_0)v_x(j+t_0)$$

and hence

$$E((x(t+t_0) - x(t_0))^2)/t = \sum_{i=1}^{t}\sum_{j=1}^{t} \lambda^{|i-j|}\,\sigma^2/t = \sigma^2(t + (t-1)\lambda + (t-2)\lambda^2 + \cdots)/t,$$

where σ^2 is the variance of $v(t)$. Since $0 < \lambda < 1$, for large t this approximates $\sigma^2/(1-\lambda)$. We estimate $\lambda = R(1)$ and σ^2 from the live imaging data. A complication is that the observed single time step cell displacements $v_x(c,t)$ and $v_y(c,t)$, while broadly following a normal distribution, contained a number of large outliers which appear to be due to errors in the Imaris spot tracking algorithm. Absolute values above 5µm were removed. The variance was calculated across all remaining values of $v_x(c,t)$ and $v_y(c,t)$, giving 2.43 and 2.01 µm^2/time step respectively for Hoxb7 and Six2 cells. Single time step autocorrelation on the Six2 data with outliers removed was 0.11. Applying the autocorrelation correction yielded diffusion rates of 18.2 and 16.9 µm^2/hour (7.5 time steps per hour). The simulation parameter σ_{sim} was set to 0.2, in order to provide good computational performance combined with numerical stability, implying a diffusion rate of 0.04 µm^2/simulation time step. Simulated and observed diffusion can thus be matched by setting 455.8 (Hoxb7) or 421.5 (Six2) simulation time steps per hour. The focus of the simulation is ureteric cell behaviour, so a conversion of 450 simulation time steps per hour was used.

The simulation volume was 3.4×10^7 µm^3, with $(X,Y,Z) = (680,250,200)$. The x and y dimensions were chosen to match the experimental image section dimensions, while the z dimension was chosen to be large enough to avoid edge effects and provide a substantially greater volume than the aggregate experimental data, to ensure that random variability in the simulation results was negligible compared to experimental data. We simulated 6800 ureteric

cells in this volume, corresponding to a density of 2×10^{-4} cells/μm^3, calibrated to the approximate average density of identified Cytokeratin$^+$ cells in the timecourse data (Fig. 3E).

Cell interaction effects were calibrated to allow the formation of stable cell aggregations while ensuring that the cell repulsion force is sufficient to maintain proper cell spacing. Poor calibration of spacing distance will result in incorrect cluster density, while poor balance between adhesive and repulsive forces may result in an unrealistic collapse of larger simulated clusters. Either effect will bias the simulated progression of clustering, as the probability of collision between clusters is related to volume. The calibration of cell interaction forces was informed by the measured distances between Cytokeratin$^+$ cells (Fig. S2D), but based primarily on plots of cluster size (number of cells) versus cluster volume (Fig. S2E). This is to ensure realistic cluster density across the full range of cluster sizes. Nearest neighbour distances are more variable for experimental than simulated data, possibly due to biological variability or imprecision in image analysis, but this has little effect.

Supplementary Figures

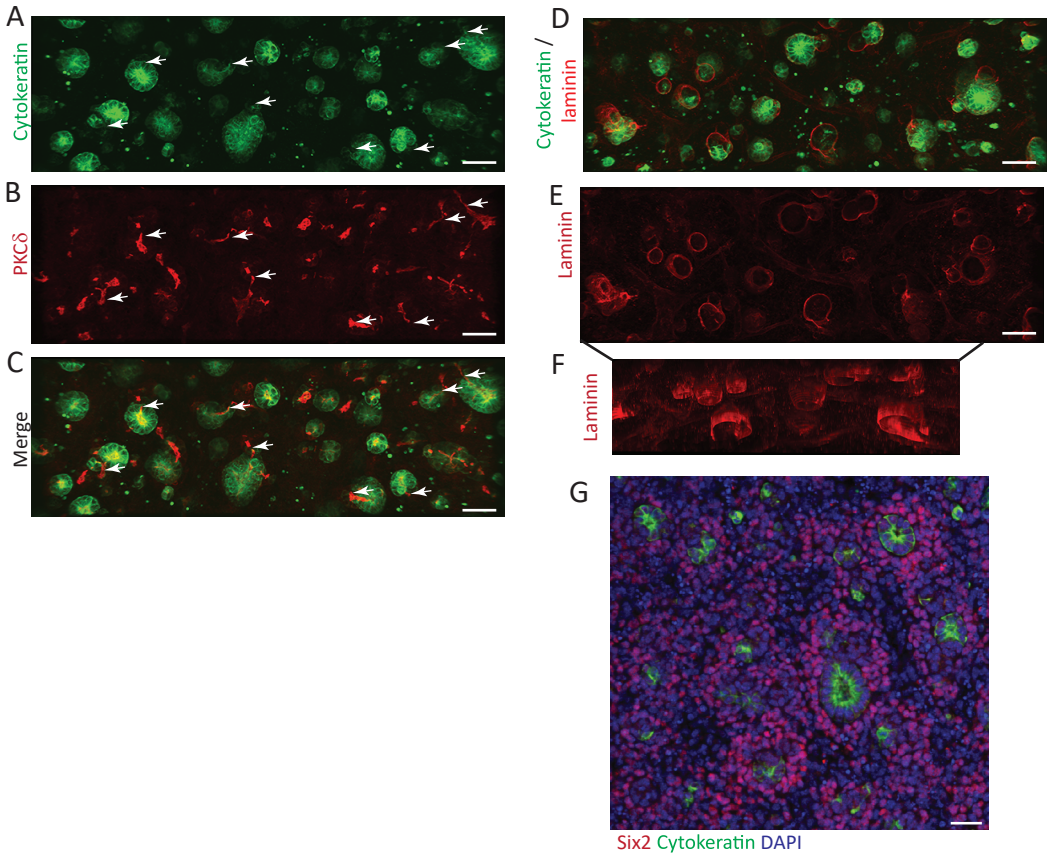

Supplementary Figure 1. Low magnification images of morphogenetic events within reaggregation cultures. A-C. Immunofluorescent labelling of early nephron formation after 24 hours of culture. **A**. UE, cytokeratin – green; **B.** Apical surface of epithelium of UE and nephron, PKCδ –red. **C.** Merge. White arrows indicate evidence of nephrons with connections to UE based upon apical staining of PKCδ. Scale bar 100μm **D-F.** Formation of basement membrane around UE and attached early nephron. **D.** UE, cytokeratin (green) and pan laminin-labelled basement membrane (red). **E.** Pan laminin (red). **F.** Z-stack of pan-laminin staining illustrating intact basement membrane around UE and forming nephrons. Scale bar 100μm. **G.** Relative localisation of UE and CM cells 24 hours post reaggregation. UE (cytokeratin; green); CM (Six2; red). Scale bar 50μm

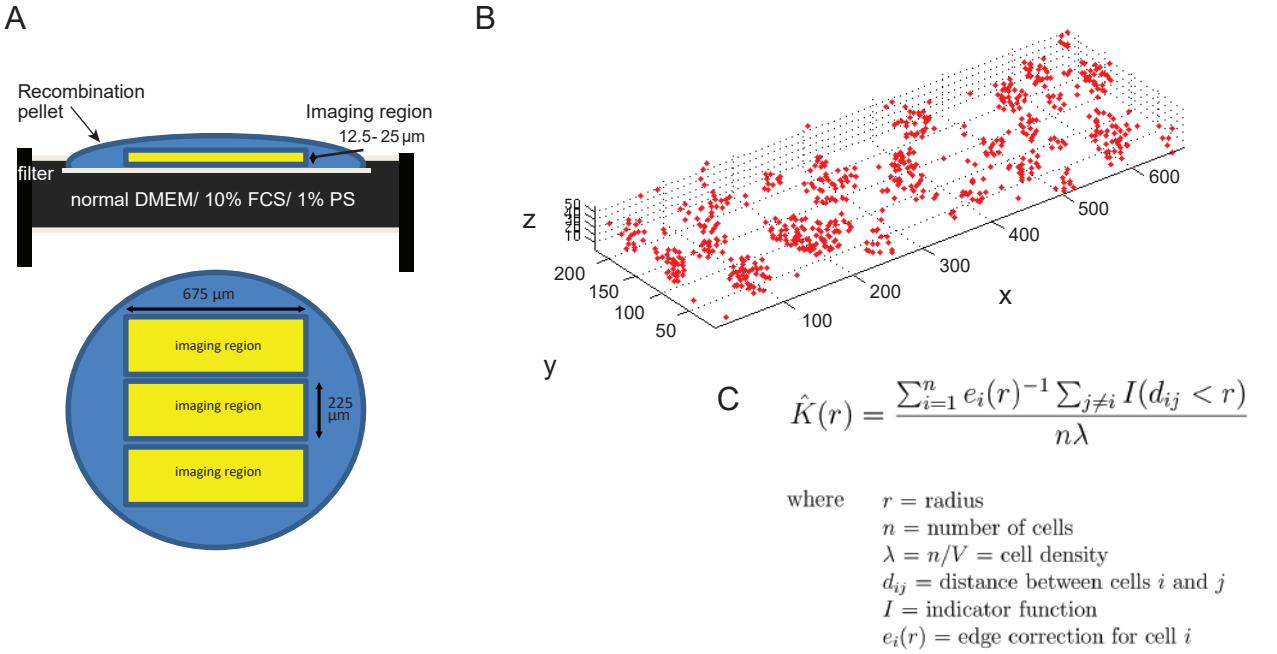
A
Recombination pellet
Imaging region 12.5- 25 µm
filter
normal DMEM/ 10% FCS/ 1% PS
675 µm
imaging region
imaging region
imaging region
225 µm
B
z
x
y
C
$\hat{K}(r) = \frac{\sum_{i=1}^{n} e_i(r)^{-1} \sum_{j \neq i} I(d_{ij} < r)}{n\lambda}$
where
r = radius
n = number of cells
$\lambda = n/V$ = cell density
d_{ij} = distance between cells i and j
I = indicator function
$e_i(r)$ = edge correction for cell i
D
Cytokeratin+ cell spacing
Proportion of cells
Nearest neighbour distance (µm)
hours culture
2
8
12
24
48
E
Cluster density
Experimental timecourse
Simulation
Cluster volume (µm³)
Cells per cluster
Cells per cluster
F
Sensitivity analysis
Standard settings
No non-adhesive cells
25% fewer UE cells
Immediate adhesion
1/10th adhesion
Mean cluster size
Hours reaggregation

Supplementary Figure 2. Quantification of clustering within reaggregation cultures and model calibration and sensitivity analysis. A. Diagram of how an explant was sampled for quantification. **B.** Sample RipleyGUI output. Cytokeratin^{+} cell positions identified in an image region from a 24hr reaggregation and imported into RipleyGUI for $K(r)$ calculation. **C.** Ripley's K formula, estimating the average number of other cells within distance r of a reference cell, divided by overall cell density (Hansson et al, 2013). **D.** Distribution of nearest neighbour distances in Cytokeratin timecourse data, used to select the clustering threshold of $12\mu m$. As clustering progresses, the proportion of cells at distances above this threshold falls consistently. This threshold was used to identify clusters in the experimental data and was also used in the calibration of simulated cell interaction forces. **E.** Scatter-plot of cluster size (measured in number of cells) against volume, experiment and simulation. The relationship is similar for the experimental and simulation data. This was used for the calibration of simulated cell interactions (adhesion, and repulsion due to spatial exclusion). **F.** Consistency and sensitivity analysis. Plots of mean cluster size versus simulated reaggregation time, for standard settings and 4 variants, each with three runs to demonstrate consistency. Clustering is insensitive to the presence of non-adhesive cells, but sensitive to the density of adhesive cells. This may explain most experimental variability in clustering. The propensity of UE cells to form adhesive bonds could not be directly measured, and clustering is also sensitive to large variation in this parameter.

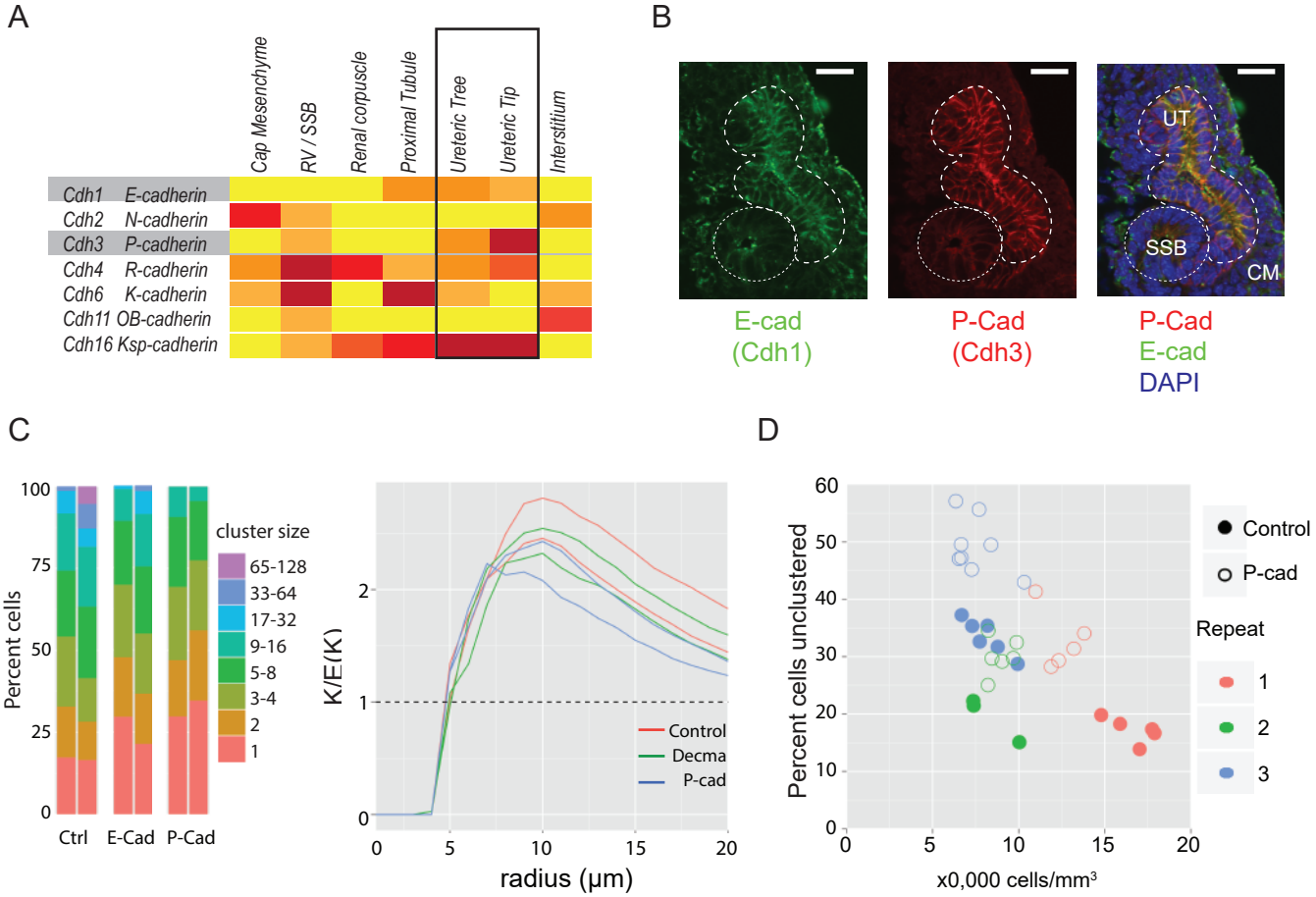

Supplementary Figure 3. Comparative distribution of cadherins during kidney development and effect of blocking antibodies to E-cadherin and P-cadherin on self-organisation. A. Expression of the major cadherins present in the mouse developing kidney displayed as a heat map of gene expression across 7 cell compartments. Cadherins are listed by gene name and common protein name. Box highlights expression within the ureteric epithelial compartments. Data was extracted from www.gudmap.org. RV, renal vesicle; SSB, S-shaped body. **B**. Immunofluroescence of E-cadherin (DECMA antibody, green) and P-cadherin (red) in cortical sections of the 13.5dpc developing kidney. CM, cap mesenchyme; SSB, S-shaped body; UT, ureteric tip. DAPI (blue). Scale bar 30μm. **C.** DECMA and P-cad results at 8hr as K/E(K) and cluster sizes. Strongest reduction in clustering produced by p-cad inhibition. **D.** Plots of cell density versus proportion of unclustered UE cells between control (solid circles) and anti-P-cadherin antibody treated (open circles) cultures from 3 different 8hr experiments. In all instances, anti-P-cadherin antibody treated cultures show a higher number of unclustered UE cells. **E, F**. Sample images from P-Cad inhibition experiment showing control (E) and experimental (F) groups at 8 and 24 hours. Immunofluorescence for cytokeratin (green) and Six2 (red) was used to identify UE and CM-derived cells respectively; DAPI (blue) marks nuclei. Scale bar 30μm.

Supplementary movies:

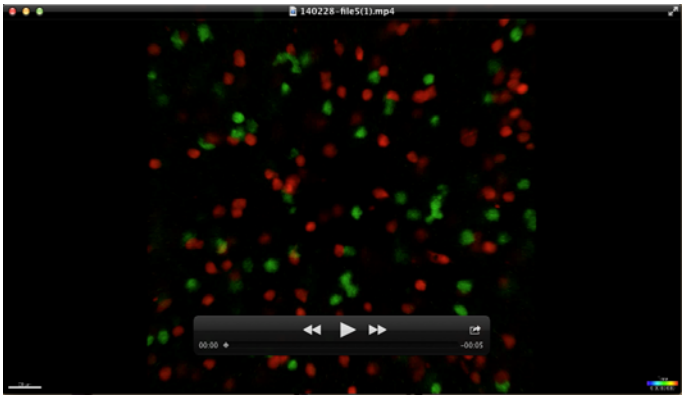

Movie 1. Timelapse imaging of reaggregation culture showing ureteric and cap mesenchyme cells. The movie depicts a single optical slice imaged across a 7 hour period commencing 2 hours after reaggreation. Red cells represent Six2-tdTomato cap mesenchymal cells. Green cells represent Hoxb7-GFP+ ureteric epithelial cells. Note that the green cells move out of field with time.

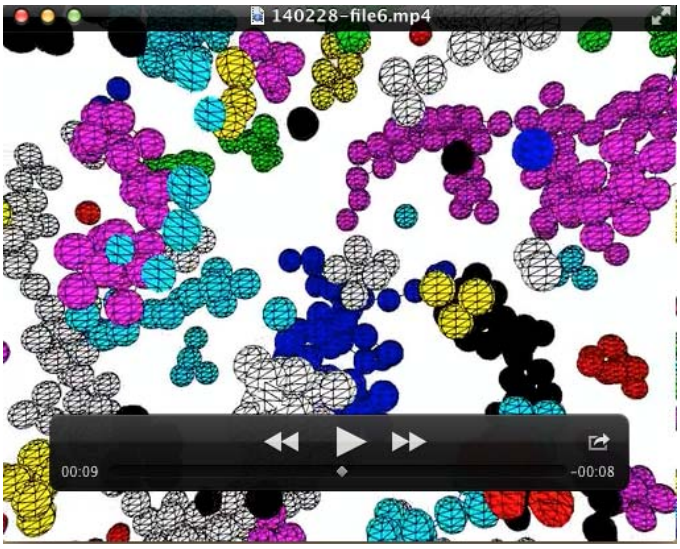

Movie 2. Clustering simulation based on a model of differential adhesion. Shows 48 hours of simulated clustering, sampled every 20 time steps. Only ureteric epithelium (adhesive) cells in a portion of simulation shown. Random colours are used to distinguish clusters, and similarity in colours between clusters has no meaning. See Fig. 4A, Fig. S2D-F and online methods for description and derivation of model. A cluster is defined as a set of cells where any two cells are connected by a path consisting of one or more adhesion bonds. Colour changes mark the joining of clusters; for example at 15 seconds the main black and blue clusters merge.